

JGR Solid Earth

RESEARCH ARTICLE

10.1029/2024JB029479

Key Points:

- We have compiled a high-resolution seismic event catalog with anthropogenic and natural sources better separated around the southern Anninghe fault
- A reliable focal mechanism inverted using dense seismic records agrees well with the geologically inferred fault orientation and slip direction
- Ground motion amplifications are obvious and frequency-dependent around fault traces, suggesting distributed damage zones at shallower depths

Supporting Information:

Supporting Information may be found in the online version of this article.

Correspondence to:

H. Yang,
hyang@cuhk.edu.hk

Citation:

Song, J., Yang, H., & Yao, H. (2024). High-resolution seismicity and ground motion variability across the highly locked southern Anninghe fault with dense seismic arrays and machine learning techniques. *Journal of Geophysical Research: Solid Earth*, 129, e2024JB029479. <https://doi.org/10.1029/2024JB029479>

Received 6 MAY 2024
Accepted 12 AUG 2024

Author Contributions:

Conceptualization: Junhao Song, Hongfeng Yang
Data curation: Hongfeng Yang, Huajian Yao
Formal analysis: Junhao Song, Hongfeng Yang
Funding acquisition: Hongfeng Yang
Methodology: Junhao Song
Project administration: Hongfeng Yang, Huajian Yao
Resources: Hongfeng Yang, Huajian Yao
Supervision: Hongfeng Yang
Visualization: Junhao Song

© 2024 The Author(s).

This is an open access article under the terms of the [Creative Commons Attribution-NonCommercial License](https://creativecommons.org/licenses/by-nc/4.0/), which permits use, distribution and reproduction in any medium, provided the original work is properly cited and is not used for commercial purposes.

High-Resolution Seismicity and Ground Motion Variability Across the Highly Locked Southern Anninghe Fault With Dense Seismic Arrays and Machine Learning Techniques

Junhao Song¹ , Hongfeng Yang^{1,2} , and Huajian Yao³

¹Department of Earth and Environmental Sciences, The Chinese University of Hong Kong, Shatin, China, ²Shenzhen Research Institute, The Chinese University of Hong Kong, Shenzhen, China, ³Laboratory of Seismology and Physics of Earth's Interior, School of Earth and Space Science, University of Science and Technology of China, Hefei, China

Abstract Fault activity and structure are important factors for the assessment of seismic hazards. The Anninghe fault is one of the most active strike-slip faults in southwestern China but has been experiencing seismic quiescence for $M > 4$ earthquakes since the 1970s. To understand better the characteristics of its highly locked southern segment, we investigate seismicity and ground motion variability using recently deployed multi-scale dense arrays. Assisted by machine learning (ML) seismic phase picking and event discrimination models, we first compile a high-resolution catalog of local seismic events. We find limited earthquakes that occurred on the Anninghe fault, consistent with its generally acknowledged high locking degree. Whereas, most newly detected events appear within off-fault clusters, among which four are closely related to anthropogenic activities (e.g., mining blasts), and two neighboring faults host the remaining ones. We further apply an ML-based first-motion polarity (FMP) classifier and successfully obtain a reliable small earthquake focal mechanism, which agrees well with the geologically inferred north-south trending and eastward dipping of the Anninghe fault. Analyses of ground motion variations along two across-fault linear arrays show abrupt changes in FMPs and obvious frequency-dependent site amplifications near the mapped fault traces. It further suggests that, at finer scales, the damaged Anninghe fault zone may have split into two smaller damaged zones at shallower depths, resulting in a typical “flower-type” fault structure. The efficient workflow developed in this study can be well applied for the longer-term monitoring and better characterization of the southern Anninghe fault, or other similar regions.

Plain Language Summary The Anninghe fault in southwestern China has great potential to produce devastating earthquakes. However, its southern segment has experienced seismic quiescence during the past 40 years, resulting in less knowledge about its detailed seismicity and structures which are crucial for seismic hazard assessment. Here, we apply a series of novel machine learning methods to seismic data of multi-scale temporary dense arrays we deployed near the southern segment of the Anninghe fault. Our event detection and location results show that earthquakes along this segment are very limited, consistent with the well-acknowledged highly locked fault plane status. The detected seismic events are mostly located off the fault and many are closely related to human activities (e.g., mining explosions). The source parameters of one on-fault earthquake agree with the geologically inferred fault orientation and slip direction. The dense across-fault recordings from local and regional sources reveal much larger amplitudes around the mapped fault traces, corresponding to two shallower fault damage zones that can trap seismic energies and promote earthquake ruptures. The efficient methods used here can be extended to future longer-term seismic experiments over the Anninghe fault, or other similar faults.

1. Introduction

Fault zones (FZs) are generally composed of one or multiple high-strain core layers, surrounded by low-velocity zones (LVZs) of damaged rocks (Ben-Zion & Sammis, 2003; Faulkner et al., 2010; Yang, 2015), according to observations from exhumed faults and drilling into seismogenic faults (e.g., Chester et al., 1993; H. Li et al., 2013). FZ structures in the subsurface can have significant effects on ground motions (e.g., Ben-Zion & Aki, 1990; Kurzon et al., 2014; Qiu et al., 2020) and earthquake rupture behaviors (e.g., Dor et al., 2006; Wei et al., 2011; Weng & Yang, 2017; Weng et al., 2016). For example, the damaged FZ could promote rupture propagation of earthquakes, and such effects will increase with its width and depth (Weng et al., 2016). X. Chen

Writing – original draft: Junhao Song
Writing – review & editing:
Junhao Song, Hongfeng Yang,
Huajian Yao

and Yang (2020) also found that near-field ground velocities amplified by the LVZ may result in biased estimations of frictional properties on seismogenic faults. Therefore, imaging FZ structures with higher resolution to advance our knowledge of earthquake physics and improve the assessment and mitigation of seismic hazards has received increasing attention in recent years (Yang et al., 2021).

Many seismological methods have been successfully applied in deriving fault zone properties. As earthquakes generally occur along faults, their high-precision locations such as those relocated with double-difference methods (e.g., Trugman & Shearer, 2017; Waldhauser & Ellsworth, 2000) have been commonly utilized to infer fault geometries at seismogenic depths (e.g., H. Chen et al., 2022; Z. Jia et al., 2023; McGuire & Ben-Zion, 2005; Ross et al., 2019). Apart from spatial distributions, focal mechanisms of earthquakes can also provide strong constraints on fault orientations and slip directions (e.g., H. Chen et al., 2021; Yang et al., 2009). The velocity reduction within the damaged FZ and velocity contrast across the fault bimaterial interface can produce FZ trapped waves and head waves, respectively (Ben-Zion, 1998). High-frequency body waves may also be reflected and diffracted from the boundary of LVZs (Yang & Zhu, 2010). Systematic analyses and modeling of these FZ-related waves have been conducted in numerous studies. As examples, Share et al. (2023) recently developed a novel tool to detect FZ head waves and identified an ~70-km-long continuous but geometrically complex bimaterial interface with ~0% to >15% P velocity contrasts along the San Jacinto fault zone. Qiu, Ben-Zion, et al. (2021) found and imaged a trapping structure (width: ~300 m; depth: 3–5 km; Vs reduction: ~20%) within the rupture zone of the 2019 Mw 7.1 Ridgecrest earthquake by modeling the stacked FZ trapped waves of aftershocks. Besides, analyses of local site response indicate the feasibility of monitoring temporal seismic velocity changes in FZs (e.g., Wu et al., 2009) and distinguishing the potential fault damage zone embedded in the unconsolidated basin (e.g., Song & Yang, 2022). Tomographic methods based on arrival times of active or passive sources (e.g., Allam et al., 2014; Mu et al., 2024; Shao et al., 2022; Share et al., 2020), dispersion data from noise cross-correlations (e.g., Luo et al., 2023; Qiu, Niu, & Fin, 2021; Y. Wang et al., 2019), and teleseismic receiver functions (e.g., Allam et al., 2017; X. Jiang et al., 2021) also present good performance in deriving high-resolution FZ velocity models.

The Anninghe fault in southwest China, as one critical section of the left-lateral strike-slip Xianshuihe-Xiaojiang fault system that has hosted lots of devastating earthquakes (Figure 1a), plays an important role in accommodating the southeastward extrusion and clockwise rotation of lithospheric fragments in the southeastern Tibetan Plateau (e.g., Guo et al., 2023; Royden et al., 2008; Tapponnier et al., 2001; E. Wang, 1998; Wen et al., 2008). Previous geomorphic studies estimated that the strike-slip rate along the Anninghe fault since the late Quaternary is about 3–6 mm/yr, with a thrust component of about 1 and 2 mm/yr (e.g., He & Ikeda, 2007; Ren, 2014). The newly generated Daliangshan fault to the east of the Anninghe fault is currently experiencing significant sinistral shear as a result of the partitioning of the strike-slip motion on the southern end of the Xianshuihe fault, thus raising the question of whether the Anninghe fault is still the main boundary fault or not (e.g., He & Ikeda, 2007; He et al., 2008; M. Wang & Shen, 2020). The Anninghe fault has hosted several surface rupturing earthquakes in history (Figure 1c) including the 1480 M7.5 earthquake that occurred on its northern segment from Shimian to Mianning (Wen, 2000) and the 1536 M7.5 earthquake that ruptured its southern segment from Xichang to Mianning (H. Wang et al., 2014). However, both segments have elapsed time of about 500 years from the previous major earthquakes ($M \geq 7$), which is approaching the average recurrence interval of 520–800 years (e.g., Ran et al., 2008; H. Wang et al., 2014; Wen et al., 2008). Moreover, the seismic quiescence for $M > 4$ earthquakes has lasted for more than 40 years (Wen et al., 2008) and very low b-value distributions have also been observed (Yi et al., 2008) along the Anninghe fault. Crustal block modeling studies constrained by geodetic data have suggested high interseismic locking degrees along the southern segment of the Anninghe fault (e.g., G. Jiang, Xu, et al., 2015; Y. Li et al., 2021). The southern segment of the Anninghe fault is believed to be in the late stage of the interseismic period. According to dynamic rupture modeling results, it has the potential to produce another $M \geq 7$ earthquake with continuous surface ruptures (Yao & Yang, 2022). Given the high seismic potential, dense population of more than 1.5 million, and critical infrastructures in this region, monitoring the seismicity and probing finer subsurface structures of the Anninghe fault have become important tasks.

In the past decade, more than 30 broadband seismometers with an average interstation spacing of ~16 km, named the Xichang array, have been in operation around the Anninghe fault and show high detectability of earthquakes (C. Jiang, Fang, et al., 2015). Based on the routine catalog produced by this array, Feng et al. (2021) detected more earthquakes before and after the 2018 M_L 4.0 Shimian earthquake that occurred on the northernmost Anninghe fault and proposed the cascade stress triggering mechanism of its foreshock sequence. L. Zhang, Su, et al. (2022)

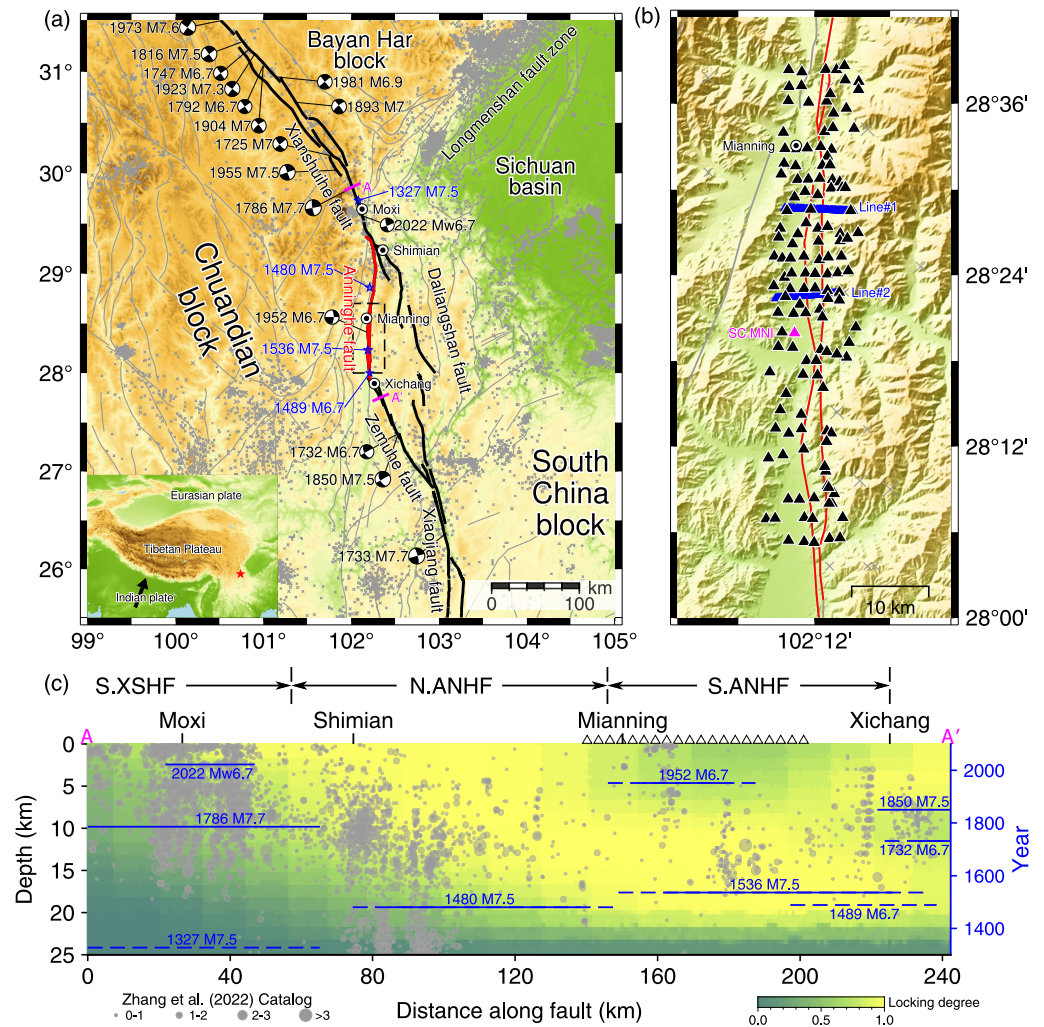


Figure 1. (a) Tectonic setting map around the Anninghe fault, which is marked by the red line. (b) Seismic stations around the southern Anninghe fault. Black triangles correspond to the rectangular array used for detection and location. The pink triangle marks the permanent broadband station SC.MNI. Blue triangles represent two dense linear arrays across the Anninghe fault. (c) The Anninghe fault status. Blue solid and dashed lines show observed and inferred rupture extends of large historical earthquakes, respectively. Gray dots are earthquakes that occurred between 2013 and 2020 (L. Zhang, Su, et al., 2022). The background colors represent locking degrees derived from crustal block modeling (Li et al., 2021). (S. XSHF: the southern Xianshuihe fault; N.ANHF: the northern Anninghe fault; S.ANHF: the southern Anninghe fault.)

systematically searched for repeating micro-earthquakes caused by regular ruptures of the same small fault asperity and suggested partitioning of deep fault slip along the southern Xianshuihe fault (~8 mm/yr), northern Anninghe fault (~1 mm/yr), and northern Daliangshan (2–6 mm/yr) after building a more complete catalog (2013–2020) with the dense Xichang array. However, the detailed seismicity of the more hazardous central and southern parts of the Anninghe fault remains poorly investigated and understood, which would require denser station coverages and more advanced methods.

In this study, based on dense seismic array recordings and advanced machine learning (ML) techniques, we aim to better investigate both the seismicity and structure of the highly locked southern Anninghe fault. In the next section, we briefly describe multi-scale dense temporary arrays deployed along the Anninghe fault zone (Figure 1b). In later sections, we first perform ML-based phase picking and then apply another ML-based seismic discrimination model to the associated local seismic events. This auxiliary discrimination step predicts the probabilities of being natural earthquakes, which are used to re-weight S phases during our location process. We show that anthropogenic events can be more precisely located and thus better separated from natural earthquakes

to avoid misinterpretation. We further apply the double-difference relocation based on cross-correlation derived travel time differences and compile a high-resolution seismic event catalog. We predict first motion polarities (FMPs) for all the well-located events using an ML-based FMP classifier and derive the reliable source parameters of a small earthquake (M_L 1.5) on the Anninghe fault. We also observe obvious and consistent FZ site effects based on denoised waveforms from the detected larger anthropogenic events. The standard spectral ratio (SSR) method is finally applied to help better constrain the shallower fault zone structure. Based on our high-resolution results, we discuss the slip characteristics and subsurface structures of the southern Anninghe fault, and implications for monitoring seismicity and fault properties over regions of similar settings.

2. Dense Seismic Array Data

Multi-scale dense seismic arrays were deployed along and across the highly locked central and southern portions of the Anninghe fault between October 2019 and March 2020 (Figure 1b). Previous active and passive source tomography studies with this data set have obtained higher-resolution fault zone structures (e.g., Luo et al., 2023; Mu et al., 2024; Shao et al., 2022). In this study, we first detect and locate local seismic events using the rectangular dense array that has dimensions of ~ 10 km \times ~ 60 km and consists of 134 3C short-period (5 s) QS-5A instruments with a sampling rate of 100 Hz. The data availability of this array (hereinafter referred to as the Anninghe array) is shown in Supporting Information S1 (Figure S1). In the meantime, two ultra-dense linear arrays were deployed almost perpendicularly across the Anninghe fault zone. The northern (Line1) and southern (Line2) linear arrays consist of 129 and 88 3C short-period (10 s) QS-10 instruments, respectively. Both profiles span the fault zone with an aperture of ~ 8 km and present denser station coverage near the mapped fault surface traces (~ 50 m). Previous studies with similar array configurations (e.g., Z. Zhang, Deng, et al., 2022) suggest that excessive amounts of seismic phases from such ultra-dense linear arrays may significantly affect the accuracy of seismic event locations, we thus exclude them from the detection and location processes. Instead, we make use of their dense spatial samplings to analyze ground motions generated from both anthropogenic sources and local-to-regional earthquakes for better characterization of shallow fault zone structures. One permanent broadband station, located within the Anninghe array, is utilized here as a benchmark to calibrate both the amplitude and polarity of our temporary array recordings in later sections.

3. High-Resolution Seismic Catalog Compilation

Building high-resolution seismic catalogs is fundamental to various analyses including the determination of fault geometries (e.g., Ross et al., 2019; Yang et al., 2009), interpretation of earthquake nucleation processes (e.g., Ellsworth & Bulut, 2018; Feng et al., 2021; Kato et al., 2012; G. Zhu et al., 2022), etc. During the past several decades, permanent or temporary high-quality dense seismic networks have been extensively deployed worldwide, leading to an exponential increase in seismic data volume (Arrowsmith et al., 2022). It's thus critical to effectively detect signals of interest such as earthquakes from massive continuous seismic data. One of the most popular methods is the short-term-average over long-term-average (STA/LTA) algorithm (Allen, 1978), which triggers a detection once the ratio exceeds the preset threshold. More recently, machine learning (ML) techniques have been greatly developed and proven powerful tools in seismology (Kong et al., 2019), especially in the field of automated earthquake detection and phase picking (e.g., Mousavi et al., 2020; Ross, Meier, Hauksson, & Heaton, 2018; W. Zhu & Beroza, 2019). The template matching (also called matched filter) technique, which takes waveforms from known events as templates to detect missing events that produce similar waveforms, can help further improve the catalog completeness (e.g., Shelly et al., 2007; Yang et al., 2009).

However, along with the enhanced detection ability, anthropogenic events have been increasingly reported in micro-seismicity studies (e.g., Neves et al., 2021; Woo et al., 2023; Zhou et al., 2021), even though the ML phase picking models used by these studies were trained with waveforms of tectonic earthquakes. Therefore, while investigating seismicity in regions where strong human activities exist, for example, urban or active mining areas, separating small natural earthquakes from anthropogenic events is becoming more important. Although seismic events can be discriminated by P/S amplitude ratios (e.g., R. Wang et al., 2020), the choice of thresholding parameters may be subjective, and locations and S arrivals of newly detected anthropogenic events could also have considerable uncertainties, making this traditional approach inappropriate. To overcome such limitations, a convolutional-neural-network (CNN) model trained with three-component spectrograms of both natural earthquake and anthropogenic event waveforms has been developed recently and can be applied directly after the

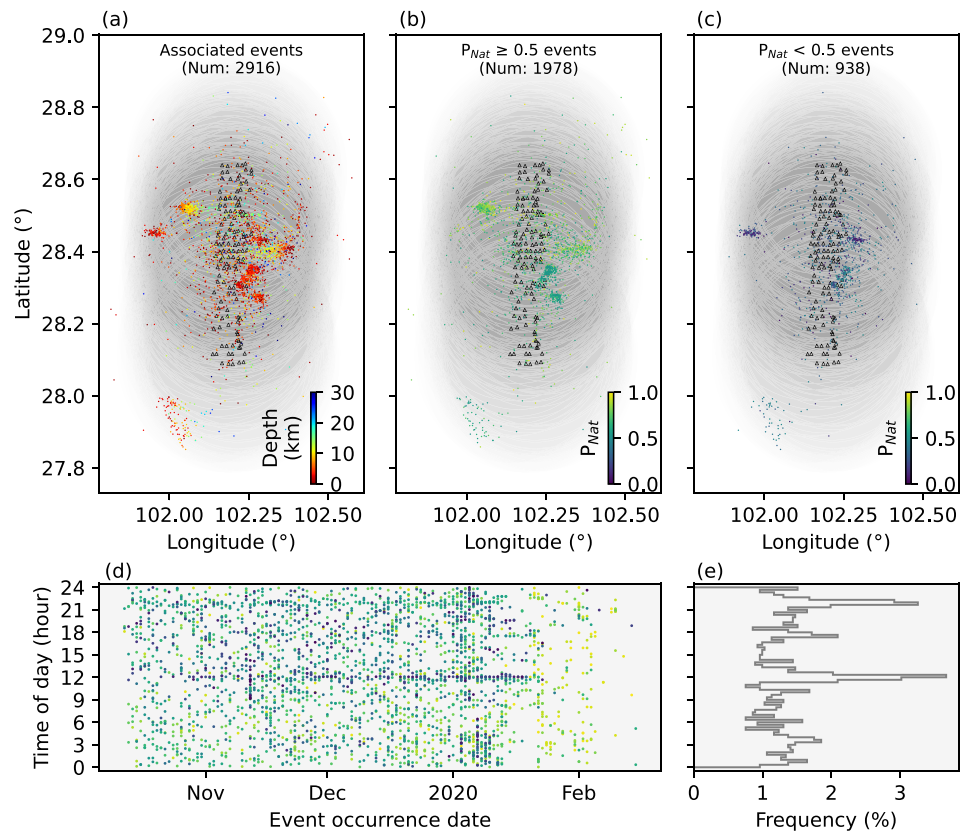


Figure 2. (a) The spatial distribution of associated events. The background shaded area marks the lateral coverage (0.3°) of individual seismic stations (black triangles). (b) The lateral distribution of natural events with color indicates the network-level natural probabilities predicted by the CNN-based discriminator. (c) The lateral distribution of anthropogenic events. (d) The temporal distribution of associated events. (e) The histogram of occurrence time of day for all the associated events.

detection step (Hourcade et al., 2023). This seismic discrimination tool has also shown versatility to different geographical regions and does not require additional customized data sets to be re-trained in most cases.

In the following subsections, assisted by the ML-based seismic phase picking and discrimination techniques described above, and the commonly used earthquake association and location methods, we aim to first compile a high-resolution catalog of local seismic events based on the dense rectangular array around the southern Anninghe fault. We also attempt to invert the focal mechanisms of the well-located events based on their first motion polarities, which are automatically determined using another ML-based FMP classifier.

3.1. ML-Based Phase Picking and Event Association

We choose the PhaseNet model (W. Zhu & Beroza, 2019) to pick P and S phase arrivals from the continuous three-component data at each station and the REAL algorithm (M. Zhang et al., 2019) to associate these phase picks into individual events. After comparing with results based on other combinations (Figures S2–S7 in Supporting Information S1), we find that PhaseNet has the advantage of picking much more potential P and S phases, and REAL can provide more stable association results, although the computational cost for REAL is relatively higher since it's based on grid searching. We retain PhaseNet phase picks above the probability threshold of 0.3, a relatively lower threshold than other studies (e.g., Tan et al., 2021), to detect as many events as possible. In the present work, a local 1D velocity model (Table S1 in Supporting Information S1) extracted and modified from the Community Velocity Model V.1.0 of Southwest China (Y. Liu et al., 2021) is used for both traveltimes calculation and subsequent event locations. While performing the REAL association, the potential location of each event is searched over 3D spatial grids up to a depth of 30 km and within 0.3° (~ 33 km) of the station that records the initiating P pick. The searching grid size in the vertical and lateral directions are 2 km and 0.02° , respectively. Only events with P and S arrivals simultaneously recorded at three or more stations are

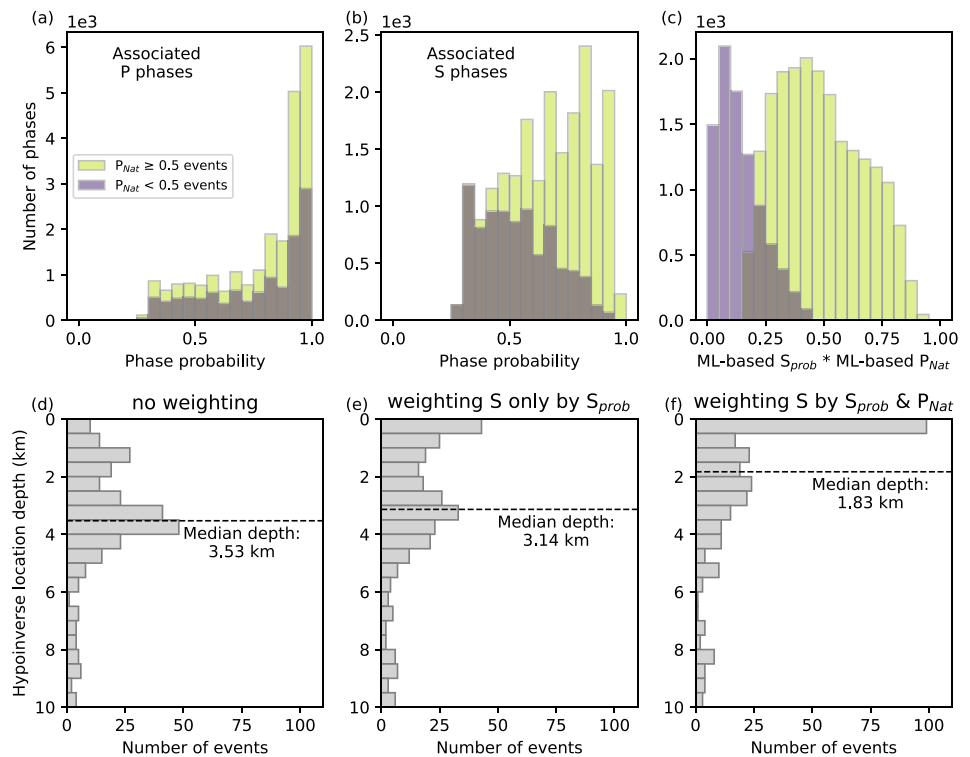


Figure 3. (a) The associated P phases for natural and anthropogenic events. (b) Similar to (a) but for associated S phases. (c) Adopted S phase weights by multiplying S phase probability and event natural probability. Depth distributions of events (d) without phase weighting, (e) with weighting by only S phase probability, and (f) with weighting by both S phase probability and event natural probability.

retained. In the end, 34,972 P and 29,002 S arrivals are associated into 2,916 events (Figure 2a). Compared to existing catalogs for the study region during the same period (Figure S8 in Supporting Information S1), we have detected many more local seismic events through the dense array and advanced phase picking model.

3.2. ML-Based Discrimination and Event Location

However, around the southern Anninghe fault, some repeated mining explosions have been previously reported by L. Zhang, Su, et al. (2022). This is also supported by the shallow depths of many associated events (Figure 2a) and evidenced by the temporal distribution of associated events (Figures 2d and 2e). To build a high-precision catalog, performing seismic event discrimination to mitigate interferences between different sources becomes necessary. The incorrect labeling and location may mislead potential analyses that rely on the spatial location of seismicity. Here we apply the well-trained CNN-based discrimination tool (Hourcade et al., 2023) to the newly detected local seismic events for automatic and effective discrimination between natural and anthropogenic events. It would predict the natural probability of waveforms recorded at each station based on three-component 60-s spectrograms and then compute the probability of each seismic event being a natural earthquake (Figure S9 in Supporting Information S1). After discrimination, two shallow clusters of events whose natural probabilities are mostly less than 0.5 have been well separated (Figure 2c). Two clusters that consist of deeper events and have overall larger natural probabilities may correspond to tectonic earthquakes (Figure 2b).

During the association step, lots of lower probability P and S picks (i.e., false positives) have been discarded and most of the associated picks have larger phase probabilities. However, although most associated P phases have higher probabilities (Figure 3a), considerably lower probability S phases are unexpectedly associated, especially for anthropogenic events (Figure 3b). Usually, S phases of anthropogenic events at shorter distances may be strongly influenced by surface waves and thus have lower probabilities and larger uncertainties (e.g., Figure 4c). When locating events, including these uncertain phase arrivals may largely affect the location results. Here, we

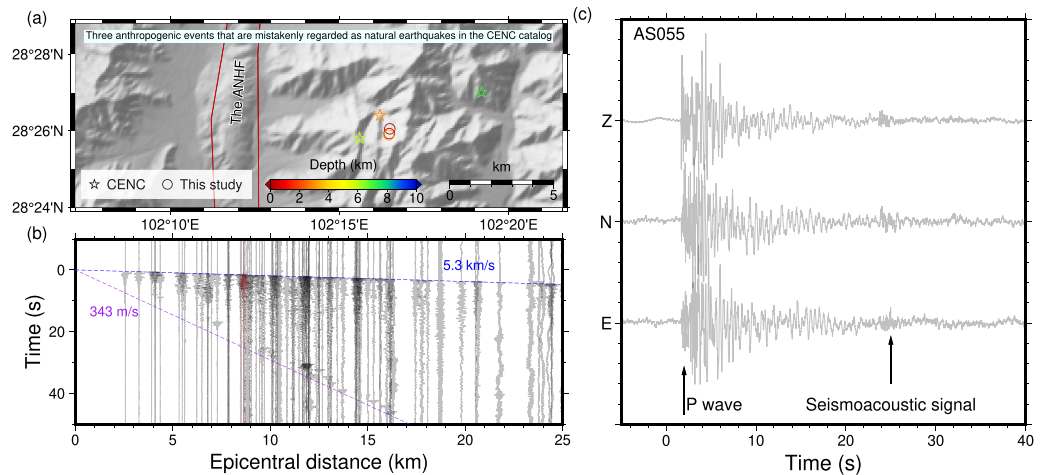


Figure 4. (a) The comparison of locations for three anthropogenic events. (b) The vertical waveform cross-section for one anthropogenic event. Note that the blue dashed line marks the P wave moveout and the purple dashed line marks the sound wave moveout. (c) Three-component waveforms at one station which is colored red in (b).

combine the ML-predicted S phase and natural earthquake probability to better weight S picks. For instance, if the event has a large probability of being a natural earthquake, its S phase weights would be close to its S phase probabilities. But if the event has a very low natural probability, its S phase weights would be greatly down-weighted. This scheme directly combines the S phase probability and event natural probability predicted from ML models and does not require manual thresholding to remove uncertain S picks.

Afterward, we locate each event based on the weighted phases with the Hypoinverse software (Klein, 2002). The location results show that anthropogenic events, which generally occur at shallow depths, have been better located close to the surface (Figures 3d–3f), indicating the effectiveness of the proposed S phase weighting scheme. For instance, we notice that within six events (occurred during 2019.10–2019.12, Figure S8 in Supporting Information S1) that are officially cataloged and labeled as natural earthquakes by the China Earthquake Networks Center (CENC), three of them are indeed anthropogenic events (Figure 4a). This is evidenced by their waveform cross-sections, which present an obvious move out of seismoacoustic signals at the velocity of around 343 m/s (Figure 4b). Compared to the CENC locations, our final catalog also presents a shallower and tightly clustered spatial distribution (Figure 4a), which indicates that our location results are more reliable and that human-related seismic events can be well separated from local natural earthquakes in this study. In general, the improved monitoring and characterization of seismic events shown here greatly benefit from the increased density of stations (Figure S10 in Supporting Information S1).

3.3. Amplitude Calibration and Magnitude Estimation

Even though ambient noise cross-correlation functions between stations have been successfully extracted based on the Anninghe array data (Luo et al., 2023), the absolute amplitude of our instrument has not been examined yet. Before measuring the local magnitude of detected events, we examine ambient noise levels of the Anninghe array recordings with the probabilistic power spectral densities (PPSD) approach used in McNamara and Buland (2004). The comparison with high and low noise models at shorter periods shows that our temporary array recordings exhibit considerably lower amplitudes, and are also distinctly inconsistent with the adjacent station SC.MNI (Figure S11 in Supporting Information S1). We attribute this issue to the incorrect gain factors in the instrument response, which has also been reported by other seismic nodal array experiments (e.g., Taira et al., 2022). To address this problem, we include another calibration factor C within the local magnitude calculation equation. As we don't have enough cataloged earthquakes recorded by our array to perform the regression analysis of all empirical parameters, we directly use the proposed standard equation (Hutton & Boore, 1987).

$$M_L = \log A + C + 1.11 \log R/100 + 0.00189(R - 100) + 3.0$$

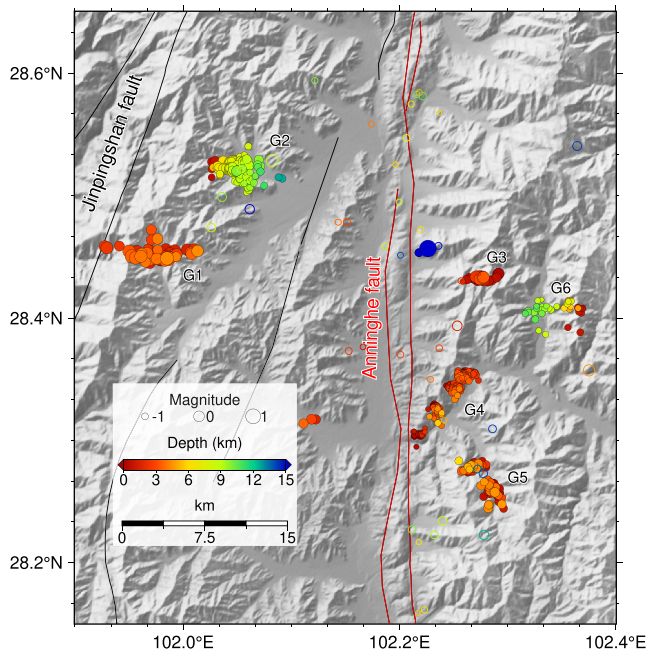


Figure 5. Spatial distribution of the well located local seismic events. Relocated events are denoted by solid dots and absolute located events with low uncertainty and enough records are shown as open circles.

in which A is the peak amplitude in mm measured from horizontal-component seismograms after removing the instrument response and then convolving waveforms with the theoretical Wood-Anderson seismometer response and R is the hypocentral distance in km. Based on a cataloged earthquake whose local magnitude (M_L) is known, after combining the measured A and R , we can derive the calibration factor at each station. We then come up with $C \approx 3.983$, averaged from all the computed calibration factors, based on which we finally calculate the local magnitudes of all the detected seismic events (Figure S11 in Supporting Information S1). By repeating the calibration process using fewer and varying stations, we find the uncertainty of this amplitude calibration factor is about 0.016 (Figure S12 in Supporting Information S1).

3.4. Event Relocation and the Final Seismic Catalog

We retain events with lower location uncertainties given by Hypoinverse (time residual <0.5 s, lateral location uncertainty <5 km, and vertical location uncertainty <10 km) and further refine the relative location of these events based on the differential travel-time relocation method. For each event pair (lateral distance <5 km), we first use FDTCC (M. Liu et al., 2022) to calculate differential travel times, in which we set the threshold of cross-correlation (CC) coefficient as 0.6. Then based on the CC-based time differences, we perform relocation with the HypoDD program (Waldhauser & Ellsworth, 2000). All the relocated events and events that are located by Hypoinverse with at least 16 arrivals and less than 1 km location un-

certainties are combined into the final catalog, which in total contains 772 events. Most events have magnitudes of around -1 (Figure S11 in Supporting Information S1) and were not previously detected. The average relative location errors are about 41 and 32 m in the vertical and horizontal directions, respectively, after repeating the relative location process 100 times and randomly selecting time difference pairs (Figure S13 in Supporting Information S1).

The spatial distribution of these well-located events reveals that most local seismic events appear within six major clusters adjacent to the Anninghe fault (Figure 5). We hereafter name these off-fault clusters from G1 to G6 for convenience. Since events are clustered by CC-based travel time differences, events within each cluster should have similar waveforms (Figures S14 and S15 in Supporting Information S1). Four (G1, G3, G4, G5) with shallower depths are attributed to anthropogenic activities, while the remaining ones (G2, G6) are comprised of tectonic earthquakes on other faults (Figures 6a and 6b). The frequency magnitude relationship within each cluster shows varying b values among different clusters (Figure 6c). Representative waveforms for each cluster are also shown in Figure 6d, from which we can see obvious differences between natural earthquake waveforms from G2/G6 and anthropogenic event waveforms from other clusters.

In addition, three anthropogenic clusters (G1, G3, G5) exhibit very concentrated temporal distributions (Figure 6b), indicating that they are closely related to human activities. Notably, natural probabilities predicted for events from G5 are relatively larger and shouldn't be solely used to separate them from natural earthquakes (Figure 2b). The cluster G4 shows scattered occurrence time and roughly linear distribution. We examine the satellite images around each anthropogenic cluster (Figure S24 in Supporting Information S1). We find that clusters G1, G3, and G5 appear close to mining/quarrying sites and cluster G4 is well aligned with the inferred tunnel within the mountain. Since events from G3 have generated clear seismoacoustic signals (Figures 4b and 4c), they are likely related to quarrying blasts. Two natural clusters (G2 and G6) have seismicity dipping toward the Anninghe fault. The cluster G2 consists of small earthquakes and exhibits a clear temporal gap during the deployment period. Considering the dipping trend of the seismicity, it might be an earthquake swarm that occurred on the neighboring left-lateral Jinpingshan fault. Another natural cluster G6 is comprised of even smaller earthquakes (below -1) and likely occurred on a small blind fault.

In comparison, events located beneath the Anninghe array (i.e., on the fault plane) are limited during the deployment period of ~ 3 months (Figure 5), consistent with the present high locking degree of this segment

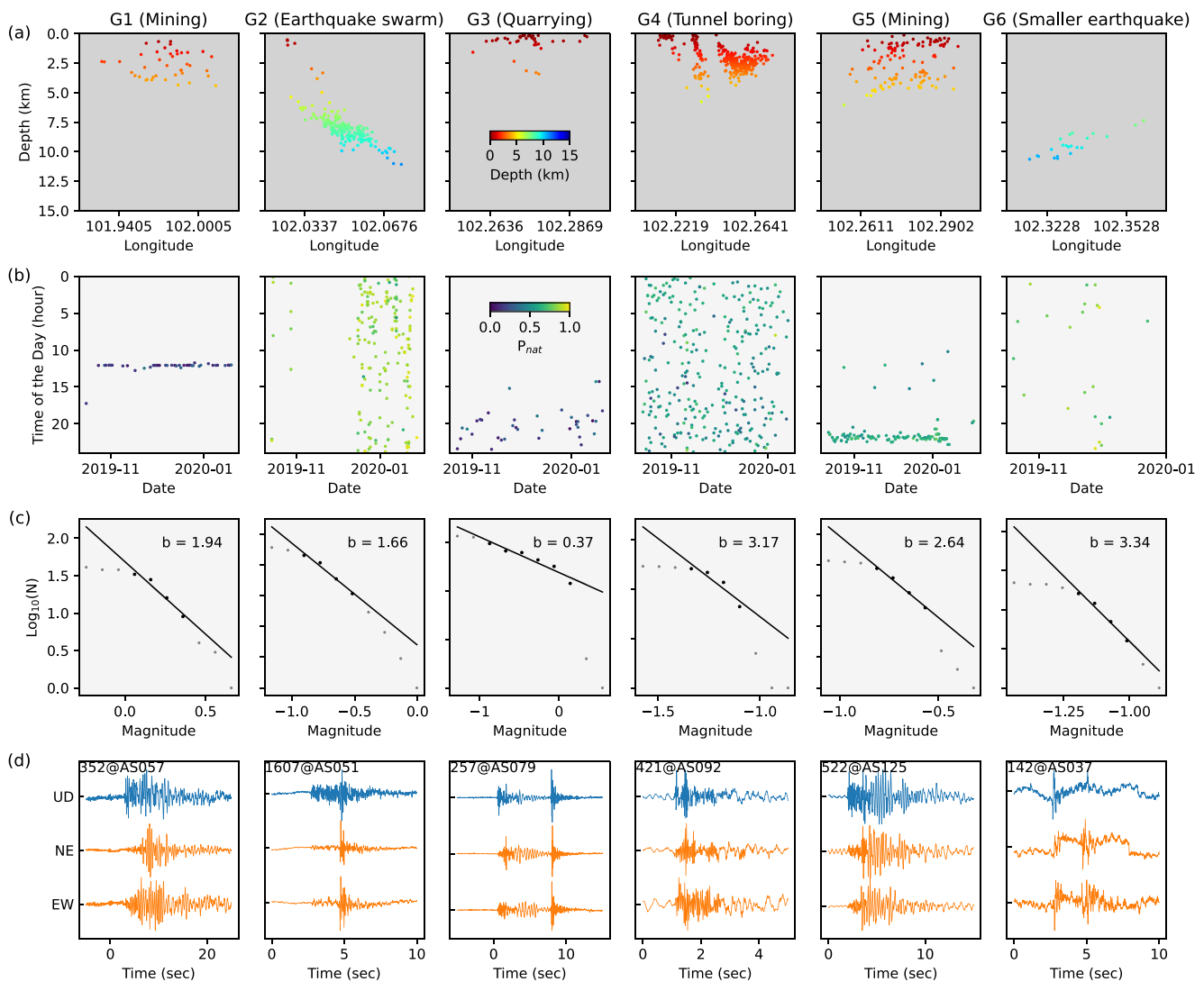


Figure 6. (a) Profile view for each group. (b) Distributions local time, color coded by P_{Nat} , for each group. (c) The frequency magnitude distribution for each group. (d) Representative three-component waveforms for each group.

suggested by previous crustal block modeling studies. Due to the lack of natural earthquakes on the Anninghe fault in our derived final catalog, we cannot resolve fault structures directly from their spatial distribution. However, this high-resolution catalog is still meaningful because it clarifies that we should revisit previous seismic catalogs built for this region more carefully before conducting any further analyses of seismicity or fault architectures.

3.5. ML-Based FMP Determination and Focal Mechanism Inversion

As mentioned before, our study region has been experiencing seismic quiescence for $M > 4$ earthquakes since 1977, indicating that the focal mechanism solution along this highly locked portion of the Anninghe fault is still unavailable in the Global Centroid Moment Tensor (GCMT) catalog. Earlier in September 1952, an M6.7 earthquake ruptured the southern central Anninghe fault around Mianning and caused severe damages including 454 fatalities and 1923 injuries. However, because of sparse modern records at that time, large discrepancies and uncertainties regarding its focal mechanism have been suggested (e.g., K. Jia & Zhou, 2012). In other words, to our best knowledge, a reliable focal mechanism solution has never been derived for the southern Anninghe fault.

Focal mechanisms of small-magnitude earthquakes can be computed from FMPs and better constrained by S/P amplitude ratios. However, manually determining P arrivals and FMPs is laborious and subjective. To solve this

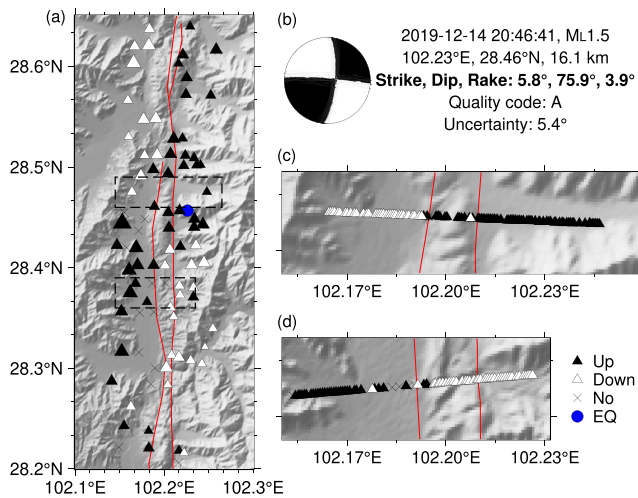


Figure 7. Polarity and focal mechanism results. (a) The blue dot marks the location of earthquake. Black and white triangles represent upward and downward first motion polarities, respectively. Crosses mean unsure polarities. (b) The inverted focal mechanism and important parameters. (c and d) The polarity results along Line1 and Line2. Red lines are the mapped fault surface traces.

problem, automatic methods such as deep learning algorithms have been recently developed (e.g., Ross, Meier, & Hauksson, 2018; Zhao et al., 2023) and successfully applied to refine the earthquake focal mechanism catalog (e.g., Cheng et al., 2023). In the present work, we first apply DiTingMotion (Zhao et al., 2023), a well-trained FMP classifier, to automatically determine FMPs of all the well-located local seismic events. First, by comparing FMPs from a teleseismic earthquake between our stations and the permanent station, we have addressed the issue of station reversal (Figure S16 in Supporting Information S1). For each event, we choose ~1.3-s long vertical component waveforms centered at P arrivals picked by PhaseNet as the input, after the prediction, we can obtain the polarity (up, down, or unknown) and sharpness (impulsive or emergent) of each P phase (Figure S17 in Supporting Information S1). Overall, event counts decrease with the total number of predicted polarities (Figure S18 in Supporting Information S1) since smaller events tend to be captured by fewer stations together with noisier recordings. The FMPs results also strongly agree with our previous interpretations that the G2 cluster consists of natural earthquakes that occurred on another left-slip fault and the G3 cluster contains explosive sources, that is, quarrying blasts (Figure S18 in Supporting Information S1).

We measure P and S wave amplitudes from three-component waveforms and calculate their S/P wave amplitude ratios. The polarity and amplitude ratio data are then used to invert focal mechanisms using the HASH program

(Hardebeck & Shearer, 2002, 2003). To ensure reliable focal solutions, the minimum polarity is eight, the maximum azimuthal gap is 90°, and the maximum takeoff angle gap is 60°. After inversion, only the focal mechanism of the largest earthquake (M_L 1.5), which fortunately occurred beneath the dense Anninghe array, has been reliably derived. This earthquake has generated the distinct first-motion polarity pattern associated with left-lateral strike-slip faulting (Figure 7 and Figure S19 in Supporting Information S1). The quality code of the derived focal mechanism is A (the most reliable class), and the uncertainty of the fault plane is about 5° (Figure 7b). The strike angle is about 5.8°, consistent with the nearly NS-trending of the Anninghe fault. The dip angle is about 76°, slightly larger than the dip angle value (70°) estimated from the previous tomographic study (Luo et al., 2023). The rake angle is about 4°, suggesting it's mainly strike-slip faulting. This small earthquake focal mechanism is consistent with the geologically determined fault orientation and slip direction. However, as we can only invert for one small earthquake focal mechanism at the depth of ~16 km, it's hard to infer the slip characteristics of the southern Anninghe fault, and it needs more local observations in the future.

4. High-Resolution Ground Motion Variations

Directly delineating the fault geometry of the Anninghe fault at seismogenic depths based on the spatial distribution or focal mechanisms of earthquakes in our final catalog is difficult due to the observed insufficient on-fault earthquakes. Fault zone structures at shallower depths are usually characterized by low-velocity zones that could amplify the incoming seismic waves and cause stronger ground motions. Previous across-fault V_p models based on active source first arrival tomography have shown different features of fault zone structures (Mu et al., 2024; Shao et al., 2022). Therefore, we try to examine ground motions from local events and local-to-regional earthquakes to further investigate shallower fault zone structures. It's well acknowledged that ground motions from seismic events are affected by, and in turn, could help constrain, various factors such as source faulting mechanisms and subsurface structures. Dense ground motion samplings across the fault zone are expected to better constrain shallow fault zone structures.

4.1. Anthropogenic Events as Potential Repeating Sources

Controlled active sources are commonly used to image the subsurface structures because their time and location of occurrences are precisely known and repeatable recordings could be produced (e.g., Mu et al., 2024; Share et al., 2020). Along the southern Anninghe fault zone, active sources (e.g., mining explosion) from two clusters have been suggested to produce repeating seismic recordings (L. Zhang, Su, et al., 2022). These anthropogenic

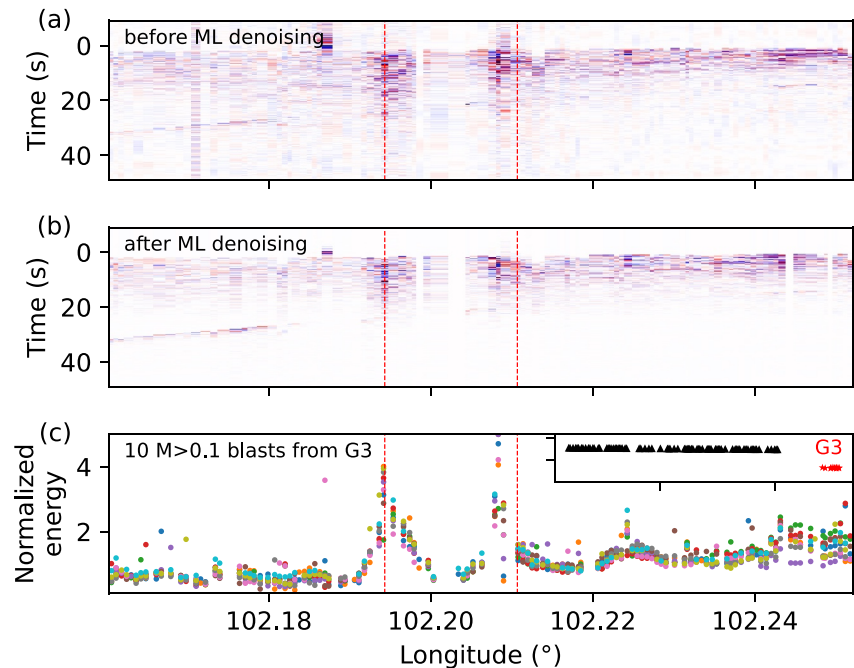


Figure 8. Ground motion variations across the fault. (a) Vertical ground motions recorded along the Line1 generated from an anthropogenic event in G3 (b) Ground motion records after denoising waveforms in (a) using DeepDenoiser (W. Zhu et al., 2019). (c) The normalized seismic energies along Line1 for 10 events from G3. Red lines are the mapped fault surface traces.

events have been better located as shown in the previous section. Because of their vicinity to the Anninghe fault, their signals could also be used to investigate the subsurface fault zone structure.

For example, the waveforms of an anthropogenic event from G3 captured by one of our dense linear arrays (Line1) have shown ground motion amplification around the mapped fault traces. We select 10 anthropogenic events with magnitudes larger than 0.1 in cluster G3 and apply the DeepDenoiser (W. Zhu et al., 2019) to their waveforms to mitigate the influence of background noises. Then we calculate the seismic energies in the first 20 s for each event and normalize them by the median value from all stations for each event. The results show that across-fault ground motion variations derived from individual anthropogenic events are overall consistent with each other. And because the sources are located adjacent to the eastern end of the linear array, seismic energies have shown an overall decaying trend westward, meaning that path effects also play an important role (Figure 8).

4.2. Frequency-Dependent Site Amplification Controlled by Damaged FZs

To eliminate the path effects and better investigate the lateral variations of shallower fault zone structures, here we quantify such seismic site amplification effects based on the across-fault linear array recordings from local and regional earthquakes following the standard spectral ratio (SSR) method (e.g., Song & Yang, 2022). The SSR method assumes the same incoming waves to the target and reference sites, and then computes the spectral ratio between them. When the bedrock sites are selected as reference sites, the spectral ratios at nearby target sites could reflect the frequency-dependent site amplifications or attenuations. Therefore, the SSR method does not require the precise source location but prefers large epicentral distances to assume similar incoming seismic waves. Since most seismic events in our final catalog have very small magnitudes and produce low signal-to-noise ratio (SNR) recordings along two linear arrays, we select candidate earthquakes based on the CENC catalog. We first choose local earthquakes with magnitudes above one and epicentral distances less than 400 km as candidate earthquakes for both linear arrays. For each candidate earthquake and each linear array, we calculate and average STA/LTA curves to examine the SNR. In the end, 11 earthquakes are selected for Line1, and 14 earthquakes are selected for Line2 (Table S2 in Supporting Information S1). Apart from producing good SNR waveforms along two linear arrays, they also generate seismic waves that nearly perpendicularly propagate to the

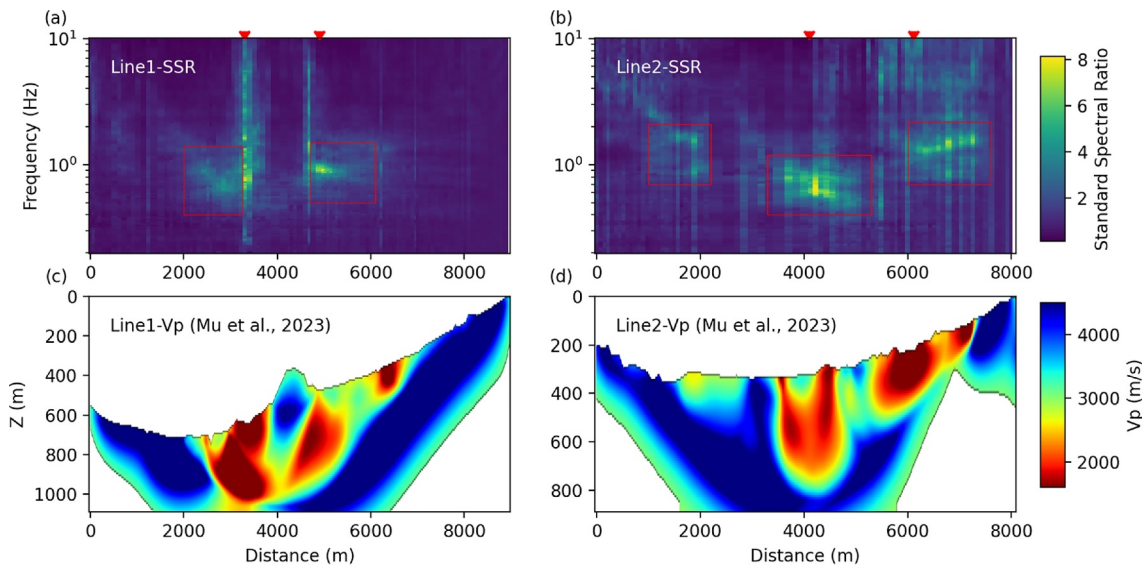


Figure 9. (a and b) Spectral ratio results for Line1 and Line2 following the spectral ratio method in Song & Yang (2022). Red inverted triangles mark the intersection locations between arrays and fault branches. (c and d) The corresponding V_p models in Mu et al. (2024).

linear array, which ensures that lateral ground motion variations are mainly caused by the heterogeneous shallower subsurface structures. Since the DeepDenoiser model was trained only using local events, it does not work well for denoising waveforms from regional earthquakes. Therefore, we have chosen the BCseis software (Langston & Mousavi, 2019) to denoise the local-to-regional earthquake recordings.

We then manually picked the phase arrivals and selected the time windows to include most P and S wave energies. We smooth the computed spectra from 0.2 to 10 Hz using the Konno-Ohmachi method with a bandwidth coefficient of 40 (Konno & Ohmachi, 1998). For each linear array, we select 10 easternmost stations as reference stations and take their averaged spectra as the reference (Figure S20 in Supporting Information S1). We then derive the spectral ratio for each earthquake. Finally, at each station, we combine the spectral ratio results of all selected earthquakes (Figure S21 in Supporting Information S1). From the SSR results, we could observe clear frequency-dependent amplification near the fault traces (Figure 9). Specifically, ground motions around the western branch of the Anninghe fault correspond to amplification at lower frequencies than the eastern branch, which is overall consistent with the inverted V_p model in Mu et al. (2024). Although the V_p structure in Mu et al. (2024) would have larger uncertainty at depth, our frequency-dependent site amplification analyses can provide another independent measurement to constrain the depth extents of different LVZs. We measure the dominant frequency (f_0) and the average velocity (V_p) for each LVZ around the fault trace, and then estimate the LVZ thickness based on the quarter-wavelength approximation (Table S3 in Supporting Information S1). By comparing with the observed LVZ thickness, which is roughly estimated from the tomographic results, the predicted values show similar depth extents for the western branch (~400 m) and the eastern branch (~200–300 m).

Compared to the previous horizontal-to-vertical spectral ratio (HVSr) study using the same linear arrays (Z. Chen et al., 2023), the SSR method proves more effective in delineating the lateral variations of shallow fault zone structures. It's worth noting that along Line1, very large ratios have been observed around both fault traces. However, after checking the satellite image and waveforms, we find that the western branch corresponds to strong amplifications while the eastern branch is associated with strong traffic noises (Figures S22 and S23 in Supporting Information S1). The SSR results based on horizontal ground motions show similar patterns but relatively lower amplitudes (Figure S24 in Supporting Information S1).

5. Discussion

Characterizing the spatiotemporal evolution of fault zone seismicity and structure with high resolution is an important task in seismology. However, this could be challenging for some highly locked and hazardous faults,

because of the lack of detected earthquakes and acquired data. For example, as an active block boundary fault in the SE Tibetan Plateau, the Anninghe fault has hosted many moderate to large devastating earthquakes in history (e.g., Wen et al., 2008). However, its southern segment has been seismically quiescent for more than 40 years, causing faulting behaviors and structures there to remain poorly understood. Taking advantage of recent dense modern instrumentations and multiple well-developed machine learning techniques, we conducted reliable seismic catalog compilation, faulting mechanism inversion, and ground motion amplification analyses and probed the detailed internal shallower structure of the southern Anninghe fault zone. Here we further discuss several aspects that may have been better addressed in this study and some implications for future investigations over the Anninghe fault zone and similar regions.

5.1. Slip Characteristics

The longer-term seismicity and interseismic coupling degree along the Anninghe fault noticeably inversely correlate with each other (Figure 1c). A repeating earthquake sequence that may reflect the aseismic slip has also been identified ~25 km south of Shimian, which is suggested to separate the northern creeping and southern locked sections (L. Zhang, Su, et al., 2022). Our local dense array has enabled us to better detect and locate two clusters of natural earthquakes on both sides of the southern Anninghe fault, with magnitude completeness of about -1.0 (Figures 5 and 6). In comparison, the paucity of earthquakes is observed on the Anninghe fault, even though the array has been deployed atop it. This is consistent with previous long-term seismicity observations and interseismic modeling results. Regarding the locking depth, high interseismic coupling has been suggested down to 15–20 km depth along the southern Anninghe fault (G. Jiang, Xu, et al., 2015; Y. Li et al., 2021). Yao and Yang (2022) had chosen to nucleate the rupture at the depth of 14 km, which is assumed to be the bottom of the seismogenic zone, while running dynamic rupture simulations along the Anninghe fault. A tiny cluster of on-fault earthquakes relocated by hypoDD and cross-correlation-derived time difference (blue solid dots near the Anninghe fault in Figure 5) is at ~16 km and some shallower (<12 km) earthquakes beneath the northern array, which show less mutual similarity and cannot be relocated, are also identified. But with near-fault observations spanning a longer term, more on-fault microseismicities including repeating earthquakes may be detected along the southern Anninghe fault to better reveal the locking and seismogenic depths.

The inverted slip deficit rate of the southern Anninghe fault can reach 10 mm/yr (e.g., G. Jiang, Xu, et al., 2015), which however may be overestimated due to the slip partitioning. Previous studies have suggested that the large left-slip misalignment of the southern Xianshuihe fault is partitioned between the Anninghe fault and the Daliangshan fault (e.g., L. Zhang, Su, et al., 2022; Figure 1a). In addition, the NE-striking Jinpingshan fault west of the Anninghe fault may also play an important role in coordinating this movement (Huang et al., 2022). First-motion polarities of earthquakes observed by our dense seismic array have illustrated the strike-slip patterns of the Anninghe fault (Figure 7) as well as another fault, probably the sinistral Jinpingshan fault (Figure S18 in Supporting Information S1), according to the dipping trend of the relocated earthquakes from G2 (Figures 5 and 6a). Unfortunately, limited by our array layout, we are unable to derive higher resolution source locations and focal mechanisms for the natural cluster G2 to better characterize the geometry and slip behaviors of the corresponding fault. Therefore, we cannot rule out the possibility of an orthogonal fault or a parallel subsidiary fault unless the location of those earthquakes is better constrained. But the spatial distributions of first motion polarity are most likely related to left-lateral strike-slip faults, which are mainly controlled by the southeastward extrusion and clockwise rotation of the lithospheric materials in the SE Tibetan Plateau.

5.2. Fault Structures

Our faulting mechanism parameters of a small on-fault earthquake are consistent with previous on-situ geological observations (e.g., Ren, 2014), suggesting that the Anninghe fault is a nearly north-south trending left-lateral strike-slip fault, together with a slight oblique component. We have also unveiled that the southern Anninghe fault dips eastward with an angle of $\sim 76^\circ$, which is similar to the dipping direction and angle ($\sim 70^\circ$) that were inferred by Luo et al. (2023). However, the interpretation of fault seismogenic structures in the southern Anninghe region based solely on seismicity should be more cautious. For instance, two repeating event clusters were previously detected to the east of the southern Anninghe fault zone but mainly consisted of small magnitude mining explosions (L. Zhang, Su, et al., 2022). However, these active sources are not well located and have larger

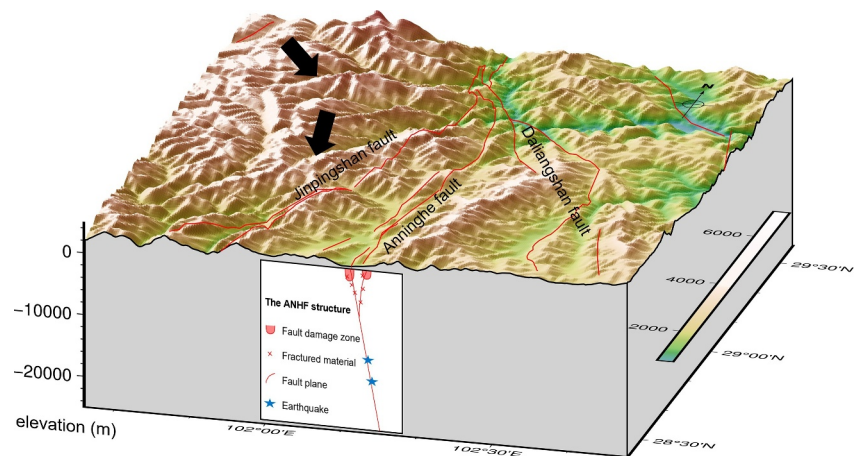


Figure 10. The schematic diagram showing the inferred structures and tectonic settings of the southern Anninghe fault.

depths, which may eventually mislead the interpretation of fault geometry. With more and more local dense arrays being deployed around the southern Anninghe fault (Lu et al., 2024), the automatic event detection and characterization methods used in this study could be a good reference for reliably compiling local seismic catalog. By deriving more high-resolution on-fault earthquakes and focal mechanisms, it may become possible to better constrain the Anninghe fault structure at seismogenic depths.

Near the surface, the Anninghe fault would divide into the western and eastern branches which are less than 3 km apart. The western branch corresponds to larger scale fault damage zones at shallower depths (Mu et al., 2024). This is also evidenced by our frequency-dependent ground motion amplification results, which show lower resonant frequency around the western fault branch along both across-fault linear arrays (Figure 9). Besides, the reversal of FMPs (i.e., opposite movement) appear near the western fault trace along both lines (Figure 7 and Figure S19 in Supporting Information S1). After denoising the recordings and carefully examining the effects of noise (Figure S22 in Supporting Information S1), we have observed very strong site amplification at 2 and 3 stations near the western branch along the Line1 (Figure 9). These results indicate that the western branch, which consists of a localized damage zone and a wider area of damaged materials, may correspond to the major fault plane. Together, the western and eastern fault damage zones form the shallow part of a low-velocity belt that has been recently imaged through ambient noise tomography (Luo et al., 2023), which failed to image them separately because of limited resolution. Weakened rock materials associated with historical earthquake ruptures may present near the fault plane and eventually result in the eastward dipping low-velocity belt down to ~8 km as imaged in Luo et al. (2023). A schematic seismotectonic model and shallower structure of the southern Anninghe fault is shown in Figure 10.

5.3. Implications for Monitoring Microseismicity

With the increasing coverage of high-quality modern seismic stations and the greatly improved seismic event/phase detection methods, the detectability of small magnitude earthquakes (i.e., micro-seismicity) has increased dramatically in recent years (e.g., Tan et al., 2021). However, in some regions, it's inevitable that anthropogenic events of similar magnitude would also be detected, which are indistinguishable by most widely used detection methods. For example, Zhou et al. (2021) applied a machine-learning-based phase picker to 1-year seismic data of a network in the Weiyuan shale gas field and detected abundant explosions that show the clear migration pattern of active seismic surveys. Similar observations have also been reported in other studies of different regions, for example, Iberia (Neves et al., 2021), South Korea (Woo et al., 2023), and so on. All these studies including the present study utilized machine-learning-based phase picking models which were trained with tectonic earthquakes (e.g., Mousavi et al., 2020; W. Zhu & Beroza, 2019), emphasizing the careful compilation of seismic catalogs based on ML techniques.

Before inferring the fault geometry or earthquake migration behavior from the spatiotemporal variations of micro-seismicity, it's important to mitigate any influences of anthropogenic sources through necessary classification

methods. For similar regions, where a variety of human-related seismic activities present, such efforts should be made to avoid wrong explanations. Several ways including the traditional S/P amplitude ratio methods, the well-trained seismic discrimination models, the spatial clustering, or temporal consistency, or even the first-motion polarities as shown in this study (e.g., Hourcade et al., 2023; R. Wang et al., 2020; Woo et al., 2023) can be utilized to separate different types of seismic events. It's also feasible to re-train the seismic discrimination model using a customized data set of anthropogenic events before it can be used for the compilation of routine catalog with more accurate labeling of event types. From this viewpoint, our catalog which consists of hundreds of confirmed anthropogenic events may also serve as the training data set. On the other hand, with sufficient repeating anthropogenic events near the Anninghe fault, it's possible to use them to monitor the temporal variations of fault properties such as seismic velocity and attenuation. But it's worth noting that the precise occurrence time and location should be first determined, for example, using the "S phase weighting" scheme that has shown good performance in this study.

6. Conclusions

The temporary dense array deployed around the southern segment of the Anninghe fault has provides an unprecedented opportunity for us to detect, if any, hidden smaller earthquakes on the fault. We performed a thorough detection of earthquakes with machine learning phase pickers. Besides, we also applied the ML-based seismic discrimination to the detected seismic events to help reduce the location errors of anthropogenic events, thus better separating them from earthquakes. We find that during the deployment period of about 3 months, earthquakes that occurred on the fault beneath our array are very limited. Nevertheless, we observed that most newly detected events are outside the Anninghe fault. Most of them are confirmed to be related to anthropogenic activities. And two clusters of natural earthquakes are identified on both sides of the Anninghe fault. The on-fault earthquakes provide us a good chance to seismologically investigate the faulting behaviors of the Anninghe fault, which agrees well with previous geological and tomographic observations. After conducting ground motion amplification analysis using dense linear array recordings across the Anninghe fault, we also noticed distinct frequency-dependent trapped energies around the mapped fault surface traces, which may correspond to shallower fault damage zones and help better constrain their spatial scales. Our study has shown the great performance of a series of ML tools in terms of probing seismicity and structure of the southern Anninghe fault together with dense seismic array data.

Data Availability Statement

The seismic phases picked from continuous data, the final catalog of local events, their three-component waveforms, the input and output data of focal mechanisms inversion, and dense linear array recordings of local-to-regional earthquakes on which this article is based are available in Song et al. (2024).

Acknowledgments

This work was supported by National Natural Science Foundation of China (U2139203), Hong Kong Research Grant Council Grants (Grants 14303721 and 14308523), State Key Lab of Earthquake Dynamics (Grant LED2021B03). We thank Song Luo (USTC) for the fault trace data and Long Zhang (CEA) for their seismic catalog. We are grateful to the Editor Satoshi Ide for the review. Constructive and detailed comments from the anonymous Associate Editor and reviewers have improved our manuscript largely. The study also benefits from additional discussions with Suli Yao (CUHK), Jinping Zi (CUHK), Weiqiang Zhu (UCB).

References

- Allam, A. A., Ben-Zion, Y., & Peng, Z. (2014). Seismic imaging of a bimaterial interface along the Hayward fault, CA, with fault zone head waves and direct P arrivals. *Pure and Applied Geophysics*, 171(11), 2993–3011. <https://doi.org/10.1007/s00024-014-0784-0>
- Allam, A. A., Schulte-Pelkum, V., Ben-Zion, Y., Tape, C., Ruppert, N., & Ross, Z. E. (2017). Ten kilometer vertical Moho offset and shallow velocity contrast along the Denali fault zone from double-difference tomography, receiver functions, and fault zone head waves. *Tectonophysics*, 721, 56–69. <https://doi.org/10.1016/j.tecto.2017.09.003>
- Allen, R. V. (1978). Automatic earthquake recognition and timing from single traces. *Bulletin of the Seismological Society of America*, 68(5), 1521–1532. <https://doi.org/10.1785/bssa0680051521>
- Arrowsmith, S. J., Trugman, D. T., MacCarthy, J., Bergen, K. J., Lumley, D., & Magnani, M. B. (2022). Big data seismology. *Reviews of Geophysics*, 60(2), e2021RG000769. <https://doi.org/10.1029/2021rg000769>
- Ben-Zion, Y. (1998). Properties of seismic fault zone waves and their utility for imaging low-velocity structures. *Journal of Geophysical Research*, 103(B6), 12567–12585. <https://doi.org/10.1029/98jb00768>
- Ben-Zion, Y., & Aki, K. (1990). Seismic radiation from an SH line source in a laterally heterogeneous planar fault zone. *Bulletin of the Seismological Society of America*, 80(4), 971–994. <https://doi.org/10.1785/bssa0800040971>
- Ben-Zion, Y., & Sammis, C. G. (2003). Characterization of fault zones. *Pure and Applied Geophysics*, 160, 677–715. https://doi.org/10.1007/978-3-0348-8010-7_11
- Chen, H., He, X., Yang, H., & Zhang, J. (2021). Fault-plane determination of the 4 January 2020 offshore Pearl River delta earthquake and its implication for seismic hazard assessment. *Seismological Society of America*, 92(3), 1913–1925. <https://doi.org/10.1785/0220200232>
- Chen, H., Yang, H., Zhu, G., Xu, M., Lin, J., & You, Q. (2022). Deep outer-rise faults in the southern Mariana subduction zone indicated by a machine-learning-based high-resolution earthquake catalog. *Geophysical Research Letters*, 49(12), e2022GL097779. <https://doi.org/10.1029/2022gl097779>
- Chen, X., & Yang, H. (2020). Effects of seismogenic width and low-velocity zones on estimating slip-weakening distance from near-fault ground deformation. *Geophysical Journal International*, 223(3), 1497–1510. <https://doi.org/10.1093/gji/ggaa385>

- Chen, Z., Yao, H., Shao, X., Luo, S., & Yang, H. (2023). Detailed sedimentary structure of the Mianning segment of the Anninghe fault zone revealed by H/V spectral ratio. *Earthquake Research Advances*, 3(3), 100232. <https://doi.org/10.1016/j.eqrea.2023.100232>
- Cheng, Y., Hauksson, E., & Ben-Zion, Y. (2023). Refined earthquake focal mechanism catalog for southern California derived with deep learning algorithms. *Journal of Geophysical Research: Solid Earth*, 128(2), e2022JB025975. <https://doi.org/10.1029/2022jb025975>
- Chester, F. M., Evans, J. P., & Biegel, R. L. (1993). Internal structure and weakening mechanisms of the San Andreas fault. *Journal of Geophysical Research*, 98(B1), 771–786. <https://doi.org/10.1029/92jb01866>
- Dor, O., Rockwell, T. K., & Ben-Zion, Y. (2006). Geological observations of damage asymmetry in the structure of the San Jacinto, San Andreas and Punchbowl faults in southern California: A possible indicator for preferred rupture propagation direction. *Pure and Applied Geophysics*, 163, 301–349. https://doi.org/10.1007/s11007-3-7643-7585-x_3
- Ellsworth, W. L., & Bulut, F. (2018). Nucleation of the 1999 Izmit earthquake by a triggered cascade of foreshocks. *Nature Geoscience*, 11(7), 531–535. <https://doi.org/10.1038/s41561-018-0145-1>
- Faulkner, D. R., Jackson, C. A. L., Lunn, R. J., Schlische, R. W., Shipton, Z. K., Wibberley, C. A. J., & Withjack, M. O. (2010). A review of recent developments concerning the structure, mechanics and fluid flow properties of fault zones. *Journal of Structural Geology*, 32(11), 1557–1575. <https://doi.org/10.1016/j.jsg.2010.06.009>
- Feng, T., Wu, J., Fang, L., Guo, X., Cai, Y., & Wang, W. (2021). Foreshocks of the 2018 ML 4.0 Shimian earthquake in the Anninghe fault and its implications for earthquake nucleation. *Seismological Research Letters*, 92(3), 1937–1949. <https://doi.org/10.1785/0220200332>
- Guo, R., Li, L., Zhang, W., Zhang, Y., Tang, X., Dai, K., et al. (2023). Kinematic slip evolution during the 2022 Ms 6.8 Luding, China, earthquake: Compatible with the preseismic locked patch. *Geophysical Research Letters*, 50(5), e2023GL103164. <https://doi.org/10.1029/2023gl103164>
- Hardebeck, J. L., & Shearer, P. M. (2002). A new method for determining first-motion focal mechanisms. *Bulletin of the Seismological Society of America*, 92(6), 2264–2276. <https://doi.org/10.1785/0120010200>
- Hardebeck, J. L., & Shearer, P. M. (2003). Using S/P amplitude ratios to constrain the focal mechanisms of small earthquakes. *Bulletin of the Seismological Society of America*, 93(6), 2434–2444. <https://doi.org/10.1785/0120020236>
- He, H., Ikeda, Y., He, Y., Togo, M., Chen, J., Chen, C., et al. (2008). Newly-generated Daliangshan fault zone—Shortcutting on the central section of Xianshuihe-Xiaojiang fault system. *Science in China - Series D: Earth Sciences*, 51(9), 1248–1258. <https://doi.org/10.1007/s11430-008-0094-4>
- He, H., & Ikeda, Y. (2007). Faulting on the Anninghe fault zone, southwest China in late Quaternary and its movement model. *Acta Seismologica Sinica*, 20(5), 571–583. <https://doi.org/10.1007/s11589-007-0571-4>
- Hourcade, C., Bonnin, M., & Beucler, É. (2023). New CNN-based tool to discriminate anthropogenic from natural low magnitude seismic events. *Geophysical Journal International*, 232(3), 2119–2132. <https://doi.org/10.1093/gji/ggac441>
- Huang, P., Gao, Y., & Xue, B. (2022). Advances in the deep tectonics and seismic anisotropy of the Lijiang-Xiaojinhe Fault Zone in the Sichuan-Yunnan Block, southwestern China. *Earthquake Research Advances*, 2(1), 100116. <https://doi.org/10.1016/j.eqrea.2022.100116>
- Hutton, L. K., & Boore, D. M. (1987). The ML scale in southern California. *Bulletin of the Seismological Society of America*, 77(6), 2074–2094. <https://doi.org/10.1785/bssa0770062074>
- Jia, K., & Zhou, S. Y. (2012). Inference of source parameters of historical major earthquakes from 1900 to 1970 in southwestern China and analysis of their uncertainties. *Chinese Journal of Geophysics*, 55(09), 2948–2962.
- Jia, Z., Jin, Z., Marchandon, M., Ulrich, T., Gabriel, A. A., Fan, W., et al. (2023). The complex dynamics of the 2023 Kahramanmaraş, Turkey, Mw 7.8–7.7 earthquake doublet. *Science*, 381(6661), 985–990. <https://doi.org/10.1126/science.adi0685>
- Jiang, C., Fang, L. H., Han, L. B., Wang, W. L., & Guo, L. J. (2015). Assessment of earthquake detection capability for the seismic array: A case study of the Xichang seismic array. *Chinese Journal of Geophysics*, 58(3), 832–843.
- Jiang, G., Xu, X., Chen, G., Liu, Y., Fukahata, Y., Wang, H., et al. (2015). Geodetic imaging of potential seismogenic asperities on the Xianshuihe-Anninghe-Zemuhe fault system, southwest China, with a new 3-D viscoelastic interseismic coupling model. *Journal of Geophysical Research: Solid Earth*, 120(3), 1855–1873. <https://doi.org/10.1002/2014jb011492>
- Jiang, X., Hu, S., & Yang, H. (2021). Depth extent and Vp/Vs ratio of the Chenghai fault zone, Yunnan, China constrained from dense-array-based teleseismic receiver functions. *Journal of Geophysical Research: Solid Earth*, 126(8), e2021JB022190. <https://doi.org/10.1029/2021jb022190>
- Kato, A., Obara, K., Igarashi, T., Tsuruoka, H., Nakagawa, S., & Hirata, N. (2012). Propagation of slow slip leading up to the 2011 Mw 9.0 Tohoku-Oki earthquake. *Science*, 335(6069), 705–708. <https://doi.org/10.1126/science.1215141>
- Klein, F. W. (2002). *User's guide to HYPOINVERSE-2000, a Fortran program to solve for earthquake locations and magnitudes (No. 2002-171)*. US Geological Survey.
- Kong, Q., Trugman, D. T., Ross, Z. E., Bianco, M. J., Meade, B. J., & Gerstoft, P. (2019). Machine learning in seismology: Turning data into insights. *Seismological Research Letters*, 90(1), 3–14. <https://doi.org/10.1785/0220180259>
- Konno, K., & Ohmachi, T. (1998). Ground-motion characteristics estimated from spectral ratio between horizontal and vertical components of microtremor. *Bulletin of the Seismological Society of America*, 88(1), 228–241. <https://doi.org/10.1785/bssa0880010228>
- Kurzon, I., Vernon, F. L., Ben-Zion, Y., & Atkinson, G. (2014). Ground motion prediction equations in the San Jacinto fault zone: Significant effects of rupture directivity and fault zone amplification. *Pure and Applied Geophysics*, 171(11), 3045–3081. <https://doi.org/10.1007/s00024-014-0855-2>
- Langston, C. A., & Mousavi, S. M. (2019). Separating signal from noise and from other signal using nonlinear thresholding and scale-time windowing of continuous wavelet transforms. *Bulletin of the Seismological Society of America*, 109(5), 1691–1700.
- Li, H., Wang, H., Xu, Z., Si, J., Pei, J., Li, T., et al. (2013). Characteristics of the fault-related rocks, fault zones and the principal slip zone in the Wenchuan Earthquake Fault Scientific Drilling Project Hole-1 (WFSD-1). *Tectonophysics*, 584, 23–42. <https://doi.org/10.1016/j.tecto.2012.08.021>
- Li, Y., Nocquet, J. M., Shan, X., & Jian, H. (2021). Heterogeneous interseismic coupling along the Xianshuihe-Xiaojiang fault system, eastern Tibet. *Journal of Geophysical Research: Solid Earth*, 126(11), e2020JB021187. <https://doi.org/10.1029/2020jb021187>
- Liu, M., Li, H., Li, L., Zhang, M., & Wang, W. (2022). Multistage nucleation of the 2021 Yangbi MS 6.4 earthquake, Yunnan, China and its foreshocks. *Journal of Geophysical Research: Solid Earth*, 127(5), e2022JB024091. <https://doi.org/10.1029/2022jb024091>
- Liu, Y., Yao, H., Zhang, H., & Fang, H. (2021). The community velocity model V. 1.0 of southwest China, constructed from joint body-and surface-wave travel-time tomography. *Seismological Society of America*, 92(5), 2972–2987. <https://doi.org/10.1785/0220200318>
- Lu, W., Zhao, Z., Yue, H., Zhou, S., Wu, J., & Song, X. (2024). The accessible seismological dataset of a high-density 2D seismic array along Anninghe fault. *Earthquake Science*, 37(1), 67–77. <https://doi.org/10.1016/j.eqs.2023.11.001>
- Luo, S., Yao, H., Wen, J., Yang, H., Tian, B., & Yan, M. (2023). Apparent low-velocity belt in the shallow Anninghe fault zone in SW China and its implications for seismotectonics and earthquake hazard assessment. *Journal of Geophysical Research: Solid Earth*, 128(3), e2022JB025681. <https://doi.org/10.1029/2022jb025681>

- McGuire, J., & Ben-Zion, Y. (2005). High-resolution imaging of the Bear Valley section of the San Andreas Fault at seismogenic depths with fault-zone head waves and relocated seismicity. *Geophysical Journal International*, *163*(1), 152–164. <https://doi.org/10.1111/j.1365-246x.2005.02703.x>
- McNamara, D. E., & Buland, R. P. (2004). Ambient noise levels in the continental United States. *Bulletin of the Seismological Society of America*, *94*(4), 1517–1527. <https://doi.org/10.1785/012003001>
- Mousavi, S. M., Ellsworth, W. L., Zhu, W., Chuang, L. Y., & Beroza, G. C. (2020). Earthquake transformer—An attentive deep-learning model for simultaneous earthquake detection and phase picking. *Nature Communications*, *11*(1), 3952. <https://doi.org/10.1038/s41467-020-17591-w>
- Mu, X., Song, J., Yang, H., Huang, J., Yao, H., & Tian, B. (2024). High-resolution shallow structure along the Anninghe Fault Zone, Sichuan, China, constrained by active source tomography. *Seismological Research Letters*, *95*(1), 408–420. <https://doi.org/10.1785/0220230137>
- Neves, M., Peng, Z., Custodio, S., Maceira, M., & Chai, C. (2021). Illuminating seismic structures in Iberia using a deep learning seismic phase detector. In *AGU Fall Meeting Abstracts* (Vol. 2021, p. T55D-0105).
- Qiu, H., Allam, A. A., Lin, F. C., & Ben-Zion, Y. (2020). Analysis of fault zone resonance modes recorded by a dense seismic array across the San Jacinto fault zone at Blackburn Saddle. *Journal of Geophysical Research: Solid Earth*, *125*(10), e2020JB019756. <https://doi.org/10.1029/2020jb019756>
- Qiu, H., Ben-Zion, Y., Catchings, R., Goldman, M. R., Allam, A. A., & Steidl, J. (2021). Seismic imaging of the Mw 7.1 Ridgecrest earthquake rupture zone from data recorded by dense linear arrays. *Journal of Geophysical Research: Solid Earth*, *126*(7), e2021JB022043. <https://doi.org/10.1029/2021jb022043>
- Qiu, H., Niu, F., & Qin, L. (2021). Denoising surface waves extracted from ambient noise recorded by 1-D linear array using three-station interferometry of direct waves. *Journal of Geophysical Research: Solid Earth*, *126*(8), e2021JB021712. <https://doi.org/10.1029/2021jb021712>
- Ran, Y., Chen, L., Cheng, J., & Gong, H. (2008). Late Quaternary surface deformation and rupture behavior of strong earthquake on the segment north of Mianning of the Anninghe fault. *Science in China - Series D: Earth Sciences*, *51*(9), 1224–1237. <https://doi.org/10.1007/s11430-008-0104-6>
- Ren, Z. (2014). Late Quaternary deformation features along the Anninghe Fault on the eastern margin of the Tibetan Plateau. *Journal of Asian Earth Sciences*, *85*, 53–65. <https://doi.org/10.1016/j.jseaes.2014.01.025>
- Ross, Z. E., Idini, B., Jia, Z., Stephenson, O. L., Zhong, M., Wang, X., et al. (2019). Hierarchical interlocked orthogonal faulting in the 2019 Ridgecrest earthquake sequence. *Science*, *366*(6463), 346–351. <https://doi.org/10.1126/science.aaz0109>
- Ross, Z. E., Meier, M. A., & Hauksson, E. (2018). P wave arrival picking and first-motion polarity determination with deep learning. *Journal of Geophysical Research: Solid Earth*, *123*(6), 5120–5129. <https://doi.org/10.1029/2017jb015251>
- Ross, Z. E., Meier, M. A., Hauksson, E., & Heaton, T. H. (2018). Generalized seismic phase detection with deep learning. *Bulletin of the Seismological Society of America*, *108*(5A), 2894–2901. <https://doi.org/10.1785/0120180080>
- Royden, L. H., Burchfiel, B. C., & van der Hilst, R. D. (2008). The geological evolution of the Tibetan Plateau. *Science*, *321*(5892), 1054–1058. <https://doi.org/10.1126/science.1155371>
- Shao, X., Yao, H., Liu, Y., Yang, H., Tian, B., & Fang, L. (2022). Shallow crustal velocity structures revealed by active source tomography and fault activities of the Mianning–Xichang segment of the Anninghe fault zone, Southwest China. *Earth and Planetary Physics*, *6*(2), 204–212.
- Share, P. E., Tábořík, P., Štěpánčíková, P., Stemberk, J., Rockwell, T. K., Wade, A., et al. (2020). Characterizing the uppermost 100 m structure of the San Jacinto fault zone southeast of Anza, California, through joint analysis of geological, topographic, seismic and resistivity data. *Geophysical Journal International*, *222*(2), 781–794. <https://doi.org/10.1093/gji/ggaa204>
- Share, P. E., Vernon, F. L., & Ben-Zion, Y. (2023). The variable continuous bimaterial interface in the San Jacinto fault zone revealed by dense seismic array analysis of fault zone head waves. *Journal of Geophysical Research: Solid Earth*, *128*(2), e2022JB025070. <https://doi.org/10.1029/2022jb025070>
- Shelly, D. R., Beroza, G. C., & Ide, S. (2007). Non-volcanic tremor and low-frequency earthquake swarms. *Nature*, *446*(7133), 305–307. <https://doi.org/10.1038/nature05666>
- Song, J., & Yang, H. (2022). Seismic site response inferred from records at a dense linear array across the Chenghai fault zone, Binchuan, Yunnan. *Journal of Geophysical Research: Solid Earth*, *127*(1), e2021JB022710. <https://doi.org/10.1029/2021jb022710>
- Song, J., Yang, H., & Yao, H. (2024). Seismic catalog and event waveform data for the Anninghe fault study (Version 3) [Dataset]. *Mendeley Data*. <https://doi.org/10.17632/6v4xj9xm2k.3>
- Taira, T. A., Dreger, D. S., & Allam, A. A. (2022). Nodal seismic experiment at the Berkeley section of the Hayward fault. *Seismological Society of America*, *93*(4), 2377–2388. <https://doi.org/10.1785/0220210372>
- Tan, Y. J., Waldhauser, F., Ellsworth, W. L., Zhang, M., Zhu, W., Michele, M., et al. (2021). Machine-learning-based high-resolution earthquake catalog reveals how complex fault structures were activated during the 2016–2017 Central Italy sequence. *The Seismic Record*, *1*(1), 11–19. <https://doi.org/10.1785/0320210001>
- Tapponnier, P., Zhiqin, X., Roger, F., Meyer, B., Arnaud, N., Wittlinger, G., & Jingsui, Y. (2001). Oblique stepwise rise and growth of the Tibet Plateau. *Science*, *294*(5547), 1671–1677. <https://doi.org/10.1126/science.105978>
- Trugman, D. T., & Shearer, P. M. (2017). GrowClust: A hierarchical clustering algorithm for relative earthquake relocation, with application to the Spanish Springs and Sheldon, Nevada, earthquake sequences. *Seismological Research Letters*, *88*(2A), 379–391. <https://doi.org/10.1785/0220160188>
- Waldhauser, F., & Ellsworth, W. L. (2000). A double-difference earthquake location algorithm: Method and application to the northern Hayward fault, California. *Bulletin of the Seismological Society of America*, *90*(6), 1353–1368. <https://doi.org/10.1785/0120000006>
- Wang, E. (1998). In *Late Cenozoic Xianshuihe-Xiaojiang, Red River, and Dali fault systems of southwestern Sichuan and central Yunnan, China* (Vol. 327). Geological Society of America.
- Wang, H., Ran, Y., Li, Y., Gomez, F., & Chen, L. (2014). A 3400-year-long paleoseismologic record of earthquakes on the southern segment of Anninghe fault on the southeastern margin of the Tibetan Plateau. *Tectonophysics*, *628*, 206–217. <https://doi.org/10.1016/j.tecto.2014.04.040>
- Wang, M., & Shen, Z. K. (2020). Present-day crustal deformation of continental China derived from GPS and its tectonic implications. *Journal of Geophysical Research: Solid Earth*, *125*(2), e2019JB018774. <https://doi.org/10.1029/2019jb018774>
- Wang, R., Schmandt, B., & Kiser, E. (2020). Seismic discrimination of controlled explosions and earthquakes near Mount St. Helens using P/S ratios. *Journal of Geophysical Research: Solid Earth*, *125*(10), e2020JB020338. <https://doi.org/10.1029/2020jb020338>
- Wang, Y., Allam, A., & Lin, F. C. (2019). Imaging the fault damage zone of the San Jacinto fault near Anza with ambient noise tomography using a dense nodal array. *Geophysical Research Letters*, *46*(22), 12938–12948. <https://doi.org/10.1029/2019gl084835>
- Wei, S., Fielding, E., Leprince, S., Sladen, A., Avouac, J. P., Helmlinger, D., et al. (2011). Superficial simplicity of the 2010 El Mayor–Cucapah earthquake of Baja California in Mexico. *Nature Geoscience*, *4*(9), 615–618. <https://doi.org/10.1038/ngeo1213>
- Wen, X., Fan, J., Yi, G., Deng, Y., & Long, F. (2008). A seismic gap on the Anninghe fault in western Sichuan, China. *Science in China - Series D: Earth Sciences*, *51*(10), 1375–1387. <https://doi.org/10.1007/s11430-008-0114-4>

- Wen, X. (2000). Character of rupture segmentation of the Xianshuihe-Anninghe-Zemuhe fault zone, western Sichuan. *Seismology and Geology*, 22(3), 239–249.
- Weng, H., & Yang, H. (2017). Seismogenic width controls aspect ratios of earthquake ruptures. *Geophysical Research Letters*, 44(6), 2725–2732. <https://doi.org/10.1002/2016gl072168>
- Weng, H., Yang, H., Zhang, Z., & Chen, X. (2016). Earthquake rupture extents and coseismic slips promoted by damaged fault zones. *Journal of Geophysical Research: Solid Earth*, 121(6), 4446–4457. <https://doi.org/10.1002/2015jb012713>
- Woo, J., Park, Y., & Ellsworth, E. (2023). Deep learning-based detection of explosions and earthquakes in South Korea. In *SSA Annual Meeting Abstracts* (Vol. 2023). <https://doi.org/10.1785/0220220087>
- Wu, C., Peng, Z., & Ben-Zion, Y. (2009). Non-linearity and temporal changes of fault zone site response associated with strong ground motion. *Geophysical Journal International*, 176(1), 265–278. <https://doi.org/10.1111/j.1365-246x.2008.04005.x>
- Yang, H. (2015). Recent advances in imaging crustal fault zones: A review. *Earthquake Science*, 28(2), 151–162. <https://doi.org/10.1007/s11589-015-0114-3>
- Yang, H., Duan, Y., Song, J., Wang, W., Yang, W., Tian, X., & Wang, B. (2021). Illuminating high-resolution crustal fault zones using multi-scale dense arrays and airgun source. *Earthquake Research Advances*, 1(1), 100001. <https://doi.org/10.1016/j.eqrea.2021.100001>
- Yang, H., & Zhu, L. (2010). Shallow low-velocity zone of the San Jacinto fault from local earthquake waveform modelling. *Geophysical Journal International*, 183(1), 421–432. <https://doi.org/10.1111/j.1365-246x.2010.04744.x>
- Yang, H., Zhu, L., & Chu, R. (2009). Fault-plane determination of the 18 April 2008 Mount Carmel, Illinois, earthquake by detecting and relocating aftershocks. *Bulletin of the Seismological Society of America*, 99(6), 3413–3420. <https://doi.org/10.1785/0120090038>
- Yao, S., & Yang, H. (2022). Hypocentral dependent shallow slip distribution and rupture extents along a strike-slip fault. *Earth and Planetary Science Letters*, 578, 117296. <https://doi.org/10.1016/j.epsl.2021.117296>
- Yi, G. X., Wen, X. Z., & Su, Y. J. (2008). Study on the potential strong-earthquake risk for the eastern boundary of the Sichuan-Yunnan active faulted-block, China. *Chinese Journal of Geophysics*, 51(6), 1151–1158.
- Zhang, L., Su, J., Wang, W., Fang, L., & Wu, J. (2022). Deep fault slip characteristics in the Xianshuihe-Anninghe-Daliangshan Fault junction region (eastern Tibet) revealed by repeating micro-earthquakes. *Journal of Asian Earth Sciences*, 227, 105115. <https://doi.org/10.1016/j.jseaes.2022.105115>
- Zhang, M., Ellsworth, W. L., & Beroza, G. C. (2019). Rapid earthquake association and location. *Seismological Research Letters*, 90(6), 2276–2284. <https://doi.org/10.1785/0220190052>
- Zhang, Z., Deng, Y., Qiu, H., Peng, Z., & Liu-Zeng, J. (2022). High-resolution imaging of fault zone structure along the creeping section of the Haiyuan fault, NE Tibet, from data recorded by dense seismic arrays. *Journal of Geophysical Research: Solid Earth*, 127(9), e2022JB024468. <https://doi.org/10.1029/2022jb024468>
- Zhao, M., Xiao, Z., Zhang, M., Yang, Y., Tang, L., & Chen, S. (2023). DiTingMotion: A deep-learning first-motion-polarity classifier and its application to focal mechanism inversion. *Frontiers in Earth Science*, 11, 1103914. <https://doi.org/10.3389/feart.2023.1103914>
- Zhou, P., Ellsworth, W. L., Yang, H., Tan, Y. J., Beroza, G. C., Sheng, M., & Chu, R. (2021). Machine-learning-facilitated earthquake and anthropogenic source detections near the Weiyuan Shale Gas Blocks, Sichuan, China. *Earth and Planetary Physics*, 5(6), 532–546.
- Zhu, G., Yang, H., Tan, Y. J., Jin, M., Li, X., & Yang, W. (2022). The cascading foreshock sequence of the Ms 6.4 Yangbi earthquake in Yunnan, China. *Earth and Planetary Science Letters*, 591, 117594. <https://doi.org/10.1016/j.epsl.2022.117594>
- Zhu, W., & Beroza, G. C. (2019). PhaseNet: A deep-neural-network-based seismic arrival-time picking method. *Geophysical Journal International*, 216(1), 261–273.
- Zhu, W., Mousavi, S. M., & Beroza, G. C. (2019). Seismic signal denoising and decomposition using deep neural networks. *IEEE Transactions on Geoscience and Remote Sensing*, 57(11), 9476–9488. <https://doi.org/10.1109/tgrs.2019.2926772>

References From the Supporting Information

- Yoon, C. E., Cochran, E. S., Vanacore, E. A., Huerfano, V., Báez-Sánchez, G., Wilding, J. D., & Smith, J. (2023). A detailed view of the 2020–2023 Southwestern Puerto Rico seismic sequence with deep learning. *Bulletin of the Seismological Society of America*, 113(6), 2377–2415. <https://doi.org/10.1785/0120220229>